Continental Shelf Research 43 (2012) 133–141

Contents lists available at SciVerse ScienceDirect

Continental Shelf Research

journal homepage: www.elsevier.com/locate/csr

Research papers

Turbulence dissipation under breaking waves and bores in a natural surf zone

F. Grasso [a,*], B. Castelle [b], B.G. Ruessink [a]

[a] Department of Physical Geography, Faculty of Geosciences, Institute for Marine and Atmospheric Research, Utrecht University, P.O. Box 80.115, 3508 TC Utrecht, Netherlands
[b] CNRS, UMR 5805 EPOC, Université de Bordeaux, Avenue des Facultés, F-33405 Talence Cedex, France

ARTICLE INFO

Article history:
Received 20 September 2011
Received in revised form
9 May 2012
Accepted 25 May 2012
Available online 7 June 2012

Keywords:
Turbulence
Bores
Nearshore processes
Breaking waves
Bed boundary layer

ABSTRACT

Wave breaking is the primary driver of beach erosion, injecting breaking-induced turbulence at the sea surface and diffusing bed boundary layer turbulence at the sea bed. The limited understanding of the vertical turbulence structure under natural breaking waves, and hence sand entrainment, is one of the reasons that coastal-evolution models produce inadequate estimates of storm response. Here we use a recently collected field dataset to analyze turbulence dissipation under breaking waves and bores on the intertidal beach at Truc Vert, France. The vertical structure of the turbulent dissipation rate indicates that wave breaking is the dominant source of turbulence dissipation. The current-induced turbulence represents no more than 50% of the turbulent dissipation rate close to the bed (at 10% of the water column), even when alongshore currents reach 1 m/s. The data further illustrate that the turbulent dissipation rate is almost depth-uniform under breaking waves, whereas it decreases profoundly toward the bed under bores. Moreover, we found that the fraction of wave energy flux decay dissipated below wave-trough level is about 1% under breaking waves and about 10% under bores. These results imply that the turbulent dissipation rate in the surf zone is severely underestimated by coastal-evolution models that do not consider breaking-induced turbulence as a surface boundary condition. Consequently, they will underestimate sand stirring and transport by mean currents during severe storms.

1. Introduction

Breaking wind-induced surface-gravity waves are the primary drivers of beach erosion during severe storms; however, our ability to predict the sometimes catastrophic loss of beach sand is limited (e.g., Ruessink and Kuriyama, 2008). Under breaking waves, turbulence is generated at both the sea surface and the sea bed (Thornton, 1979). At the sea surface, breaking-induced turbulence is injected into the water column, and may reach the sea bed (e.g., Scott et al., 2005; Hsu et al., 2006) and suspend sand intermittently (e.g., Nadaoka et al., 1988; Aagaard and Hughes, 2010). At the sea bed, in the bed boundary layer, vertical shear in oscillating and steady flows generates turbulence, which diffuses upward in the water column and results in (quasi-) periodic sand suspension (e.g., Ribberink et al., 2008; Ruessink et al., 2011). Attempts to include the effect of surface-generated turbulence in sand transport modeling have been made by, for example, Deigaard et al. (1986), Roelvink and Stive (1989), Mocke (2001) and Kobayashi et al. (2008). These models remain largely untested because of a lack of simultaneously collected data of the vertical structure of turbulence and sand suspension under field conditions. Most numerical models for coastal evolution thus apply sand-transport equations based on laboratory experiments with non-breaking waves (e.g., Ribberink, 1998; Silva et al., 2006). We believe that this is one of the main reasons why (operational) morphodynamic models struggle to make sensible predictions of sea-bed change in shallow ($< \approx 2-3$ m) water (e.g., Van Rijn et al., 2003; Ruessink, 2005; Ruessink et al., 2007; Ruggiero et al., 2009). As the first step to improve shallow-water sand transport rates and, hence, morphological evolution, we here focus on the vertical structure of the turbulence dissipation rate (often used to study surf zone turbulence) under natural breaking waves and bores.

Laboratory experiments have been seminal to improve our understanding of breaking-induced turbulence (e.g., Govender et al., 2002; Kimmoun and Branger, 2007; Scott et al., 2009; Yoon and Cox, 2010, and many others). Advanced techniques, such as Particle Image Velocimetry, have enabled to quantify the cross-shore evolution of the turbulence field beneath predominantly regular waves breaking on a planar fixed bed with unprecedented temporal and spatial resolution. This includes the vertical structure of the turbulent dissipation rate ε and hence

* Corresponding author.
E-mail addresses: f.r.grasso@uu.nl, florent.grasso@gmail.com (F. Grasso).

0278-4343/$ - see front matter © 2012 Elsevier Ltd. All rights reserved.
http://dx.doi.org/10.1016/j.csr.2012.05.014

the fraction of wave energy flux decay that is dissipated below wave-trough level. Estimates of this fraction ranged from 1% to 20%, depending on breaker type and on surf zone location (Svendsen, 1987; Ting and Kirby, 1995, 1996; Govender et al., 2004; Huang et al., 2009). Because of the use of smooth fixed beds, surface-generated turbulence is essentially the sole source of near-bed turbulence in the laboratory. In the field, where the (mobile) bed is much rougher and strong alongshore currents can be present, bed-generated turbulence is potentially more important than in the laboratory.

Due to the challenge to collect field data under harsh surf zone conditions, studies analyzing and quantifying turbulence beneath breaking waves on natural beaches are sparse. In the outer surf zone (in 4.5 m water depth), breaking-induced turbulence did not reach the bed (Trowbridge and Elgar, 2001; Feddersen and Trowbridge, 2005), whereas the vertically near-uniform turbulence intensities in shallower ($< \approx 3$ m) water depths indicated strong turbulence mixing from the surface downward (George et al., 1994). Bryan et al. (2003) estimated that approximately 10% of the wave energy flux decay must be below wave-trough level, but they lacked the observations to determine the vertical ε structure and hence to ascertain whether surface-generated turbulence is indeed the dominant source under natural conditions. Recently, Ruessink (2010) deployed a vertical array of acoustic Doppler velocimeters to characterize the vertical structure of turbulent quantities and demonstrated that the cross-shore Reynolds shear stress is due to breaking-induced vortices that transport high-speed cross-shore flow downward and disintegrate close to the bed, consistent with earlier laboratory findings (Nadaoka et al., 1989; Ting and Kirby, 1995, 1996). Occasionally, within the lower 20% of the water column, surface-generated turbulence was overwhelmed by bed-generated turbulence. Based on the same dataset, Grasso and Ruessink (2011) presented results of a preliminary study on the vertical ε structure and found it to depend on the relative wave height H_s/h (a measure of the breaking-wave intensity), with H_s the sea-swell significant wave height and h the water depth. They hypothesized the variability in ε structure to be related to whether waves were breaking or had already transformed into bores.

Here we further explore Ruessink (2010)'s dataset to investigate robustly the vertical ε structure by means of an EOF analysis, showing that the total relative wave height H_{tot}/h, which includes infragravity waves, is a better proxy for ε than H_s/h. Based on wave skewness and asymmetry estimates, we here also analyze whether breaking waves and bores indeed result in different ε magnitude and vertical structure. In addition, numerical simulations of wave breaking over our instrument array enable us to estimate the fraction of wave energy flux decay dissipated below wave-trough level and to investigate the relative importance of surface- versus bed-generated turbulence. We first describe the data and the adopted methodology; next we present and discuss our results; and finally we consider the implications of our results for sand transport modeling during severe storms.

2. Data and methods

2.1. Field experiment

The measurements were conducted at Truc Vert beach, SW France, in the framework of the "ECORS-Truc Vert 2008" field experiment (Sénéchal et al., 2011). The site is characterized by a well-developed crescentic outer bar and a smaller intertidal bar frequently intersected by rip channels (Fig. 1). An instrumented rig (Fig. 2) was positioned shoreward of the inner-bar trough to study the vertical structure of turbulence beneath waves breaking on an $\approx 1:40$ sloping, planar section of the beach. Sensors included three single-point, sideways oriented, Sontek acoustic Doppler velocimeter ocean (ADVO) probes stacked in a 0.43 m high vertical array to measure 3D flow velocities and to estimate turbulence quantities. The ADVOs shared a common logger that sampled the three sensors simultaneously at 10 Hz in one burst of 24 min, 20 s each half hour. In the design and the actual construction of the rig on the beach, special attention was paid to the positioning and orientation of all instruments to minimize disturbance of the flow field and of the bed by the instruments themselves, by the rig and by its power and logging canisters. The ADVO velocity series were quality-controlled based on the heuristic guidelines in Elgar et al. (2005) and Mori et al. (2007). Beam velocities were transformed into the ADVO's orthogonal coordinate system, which was subsequently rotated into cross-shore u, alongshore v, vertical w velocities, with positive u directed onshore, positive v to the north, and positive w upward. The elevation of the sea bed at the rig with respect to chart datum ($\approx$ mean sea level, MSL), and hence the height of each ADVO above the bed, was estimated from the sea bed echo in the simultaneously collected data of a downward-looking acoustic backscatter sensor. The pressure series at the lowermost ADVO (ADVO1) were converted to sea surface elevation, η, using linear

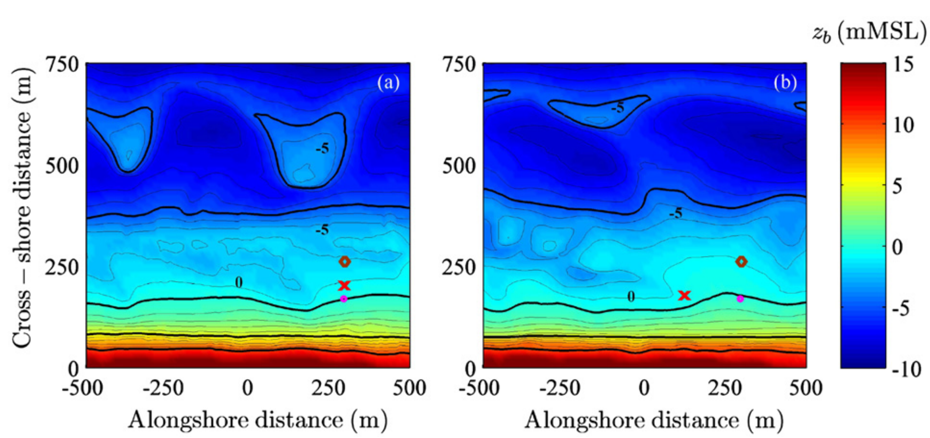

Fig. 1. Truc Vert Beach bathymetry surveyed (a) on February 14, 2008 (yearday 45), 3 weeks before the experiment and (b) on April 6, 2008 (yearday 97), 12 days after the experiment. Black thick lines represent 5-m iso-contours of bed level elevation z_b with respect to chart datum. Symbols represent rig positions during (a) yeardays 67–78.3 and (b) yeardays 78.3–85: NPS's rig (brown diamonds), our rig (red crosses), and EPOC's rig (magenta dots). (For interpretation of the references to color in this figure caption, the reader is referred to the web version of this article.)

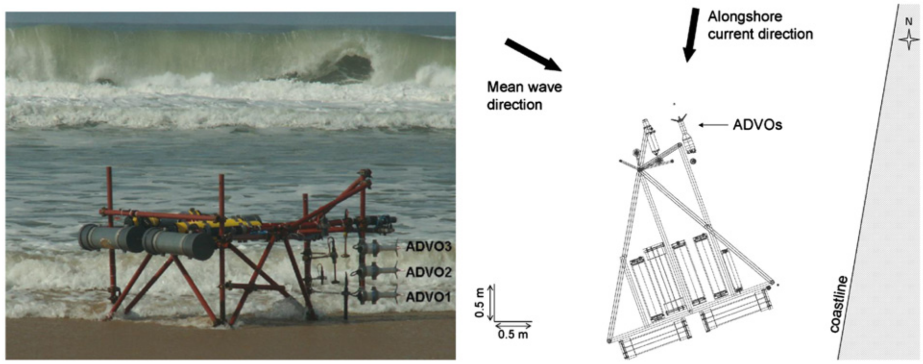

Fig. 2. Photo (left) and top-view schematic (right) of the instrumented rig deployed at the neap low-tide water level during the ECORS Truc Vert 2008 experiment. The instruments were mounted on the northwestern side of the rig to ensure that the logging and power canisters did not influence the flow field and the seabed below the sensors during conditions with waves from the west to northwest driving a southerly alongshore current. The sensing volume of the upper of the three sideways-oriented ADVOs is approximately 0.75 m above the sea bed. The image was taken at low tide on March 8, 2008 (yearday 68).

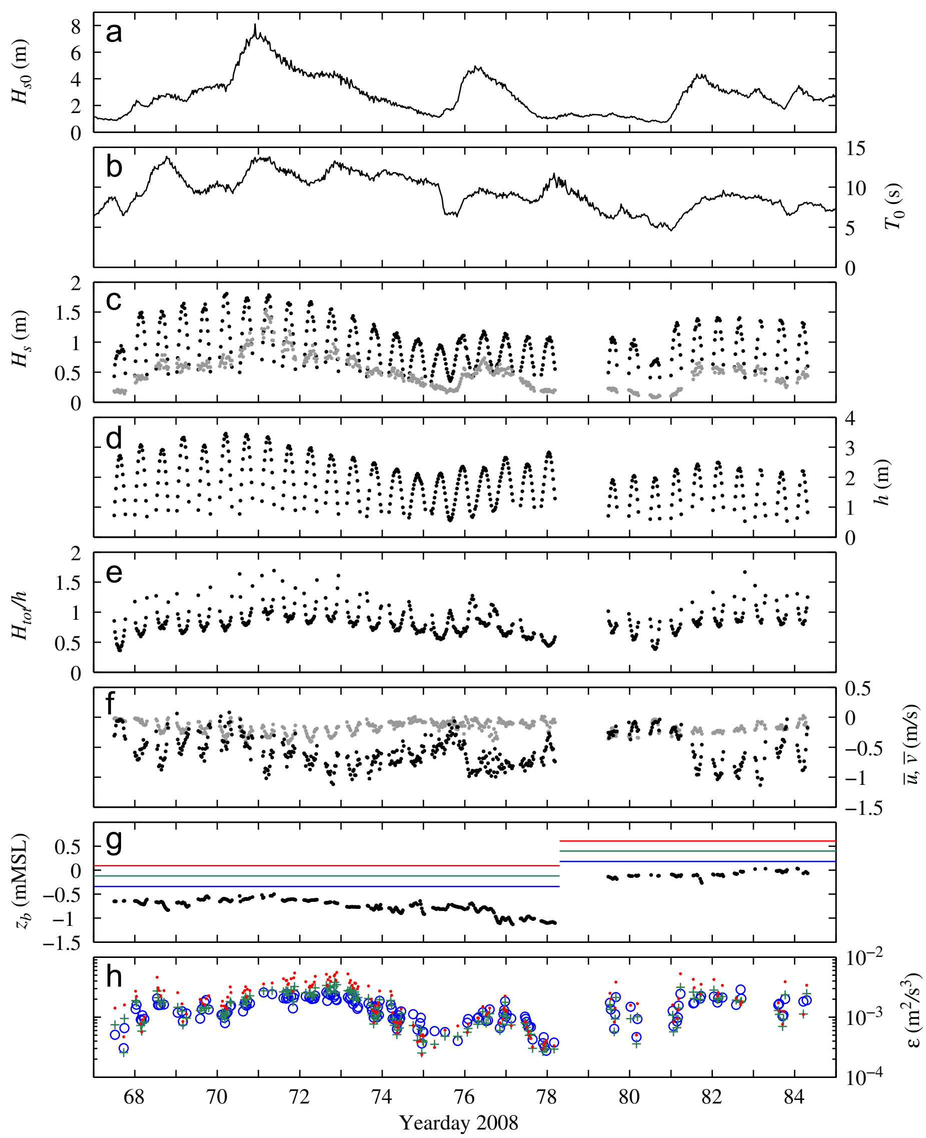

Fig. 3. Time series of offshore (a) spectral significant wave height H_{s0} and (b) wave period T_0; local (c) significant wave height H_s of the sea-swell (black, 0.04–1 Hz) and infragravity (gray, 0.004–0.04 Hz), (d) water depth h, (e) ratio of total significant wave height H_{tot} (0.004–1 Hz) to h, (f) mean cross-shore $\langle u \rangle$ (gray) and alongshore $\langle v \rangle$ (black) velocities, (g) bed level elevation z_b with respect to chart datum, and (h) dissipation rate ε at ADVO1 (circles), ADVO2 (pluses), and ADVO3 (dots). In (g), the three horizontal lines represent the elevations of the three ADVOs with respect to chart datum. The rig was repositioned on yearday 78.3 due to local beach erosion. Values in (c)–(f) are based on ADVO1.

wave theory. Further details on initial data-processing can be found in Ruessink (2010).

The rig was deployed from 7 to 30 March (yeardays 67–90) 2008. Here we focus on an 18-day period from yearday 67 to 85 during which all three ADVOs were operational. During this period, offshore (in 20 m water depth) significant spectral wave height, H_{s0}, ranged between 2 and 8 m (Fig. 3a) with wave periods, T_0, between 5 and 14 s (Fig. 3b). At the rig, the sea-swell (0.04–1 Hz) significant wave height, H_s, ranged between 0.5 and 2 m and the infragravity (0.004−0.04 Hz) H_s between 0.1 and 1.5 m (Fig. 3c).

The water depth, h, ranged between 1 and 3 m (Fig. 3d) and sea-swell H_s was depth-modulated, representative of a saturated surf zone. The total relative wave height H_{tot}/h, where H_{tot} is the total significant wave height in the 0.004–1 Hz range, varied between 0.36 and 1.7 (Fig. 3e). Waves were observed to break by both plunging and spilling, and were mostly shore-normally incident due to refraction over the seaward morphology. The burst-averaged cross-shore $\langle u \rangle$ and alongshore $\langle v \rangle$ velocities reached maximum values of −0.43 and −1.13 m/s, respectively (Fig. 3f). Measurements during positive alongshore currents (from the south) were removed to avoid flow disturbance by the rig. The bed level, z_b, at the rig varied between −1.13 and 0.03 m MSL (Fig. 3g), predominantly related to the alongshore migration of inner-bar rip channels and associated feeder channels (Almar et al., 2010). The ADVO elevations above the bed, z, ranged between 0.15 and 1.25 m.

2.2. Analysis tools

2.2.1. Turbulent dissipation rate

For each ADVO data burst, the turbulent dissipation rate ε was estimated from the high-frequency cross-shore velocity spectra $S_{uu}(\omega)$ (where $\omega = 2\pi f$ and f is frequency) with the Feddersen et al. (2007) model, as modified by Gerbi et al. (2009), that converts a wave number (k) to a frequency spectrum for frozen-turbulence in a mixed wave and mean current environment in the presence of a turbulent inertial subrange. The S_{uu} spectra were calculated using 73 s long data segments (detrended, Hamming windowed with 50% overlap) for the f=1.5–3 Hz range, in which the turbulent inertial subrange is present (Ruessink, 2010). The turbulent dissipation rate ε was calculated at 110 discrete frequencies in this frequency range using

$$\varepsilon(\omega) = \left[\frac{S_{uu}(\omega)2(2\pi)^{3/2}}{\alpha M_{uu}(\omega)}\right]^{3/2} \quad (1)$$

and then averaged to yield a single ε for each burst of ADVO data. Here, $\alpha = 1.5$ is Kolmogoroff's constant and M_{uu} is an integral over three-dimensional wavenumber space that depends on the horizontal mean flow and the wave-orbital velocities. Two quality-control tests, based on properties of the turbulent inertial subrange and proposed by Feddersen (2010), were adopted to reject bad ε estimates. The first test checks that S_{uu} has an approximate $f^{-5/3}$ roll-off in the 1.5–3 Hz range. The second test checks that the ratio of horizontal to vertical velocity spectra is near one, as expected for isotropic turbulence. About 74% of all ε estimates passed both tests, yielding 167 vertical profiles with 3ε estimates (501 individual ε estimates). As can be seen in Fig. 3h, ε ranged between 2×10^{-4} and 6×10^{-3} m^2/s^3. This is in the range of Bryan et al. (2003)'s and George et al. (1994)'s observations.

2.2.2. Wave energy flux decay

Because we have no direct observation of the wave energy flux decay, D, at the rig (e.g., from a cross-shore array of pressure sensors), we used the nearshore spectral wave model SWAN (Booij et al., 1999) to estimate D. SWAN was run in stationary mode every 30 min from yearday 67 to 85 on a 2500 m alongshore × 1400 m cross-shore computational domain with a regular 10 m spatial resolution. The simulations during yeardays 67–78.3 (yeardays 78.3–85) were run on the bathymetry surveyed on yearday 45, in Fig. 1a (yearday 97, in Fig. 1b). The intertidal computational domain was updated every day using the daily low-tide topographic surveys (Sénéchal et al., 2011). Model simulations depend on the ratio of maximum individual wave height over depth, γ. We varied γ between 0.6 and 0.75 and compared H_s at three different rigs (see symbols in Fig. 1) to find best model-data H_s agreement for $\gamma = 0.65$. At the seaward most rig, deployed in the subtidal zone by the Naval Postgraduate School (NPS, CA, USA) (Sénéchal et al., 2011) during yeardays 67–85 (see diamonds in Fig. 1), the predicted H_s agreed well with the observations with skills r^2 of 0.89 and root-mean-square errors e_{rms} of 0.27 m, even though no daily bathymetric surveys were available at this location (Fig. 4a). In the intertidal zone, the H_s predictions at the rig used in this study (see crosses in Fig. 1), and at the rig of Tissier et al. (2011), deployed by the EPOC laboratory (France) during yeardays 73–75 and 77–81 (see dots in Fig. 1), compared well with $r^2 \approx 0.91$ and $e_{rms} = 0.12$ m (Fig. 4b and c). The good H_s predictions at the rigs located on the same cross-shore profile (during yeardays 67–78.3) provide confidence in SWAN's predictions of D.

Fig. 5b presents the cross-shore profiles of D during the campaign with regard to the cross-shore beach profiles (Fig. 5a and c). The cross-shore profiles used here were alongshore-averaged over a 100 m wide alongshore domain centered around the rig. The results did not differ significantly using 50 or 150 m wide alongshore domains. Note that the daily intertidal topographies did not change significantly and the rig remained on the planar section of the beach. We observed mainly three dissipation zones: on the outer bar ($x \approx 500-800$ m) where large D values (≈ 1000 kg/s^3) were predicted, on the inner bar ($x \approx 300-400$ m), and the innermost on the intertidal beach ($x \approx 150-250$ m) where our rig was deployed. The latter dissipation zone was strongly

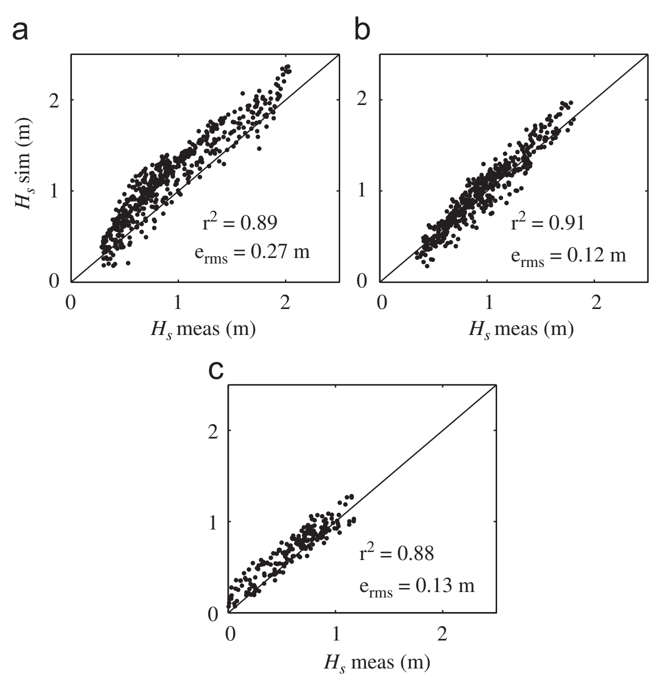

Fig. 4. SWAN simulated H_s versus measured H_s (a) at the NPS's rig, (b) at our rig and (c) at the EPOC's rig, see Fig. 1 for positions. Solid lines are the lines of equality; r^2 and e_{rms} are correlation-coefficient squared and root-mean-square error, respectively.

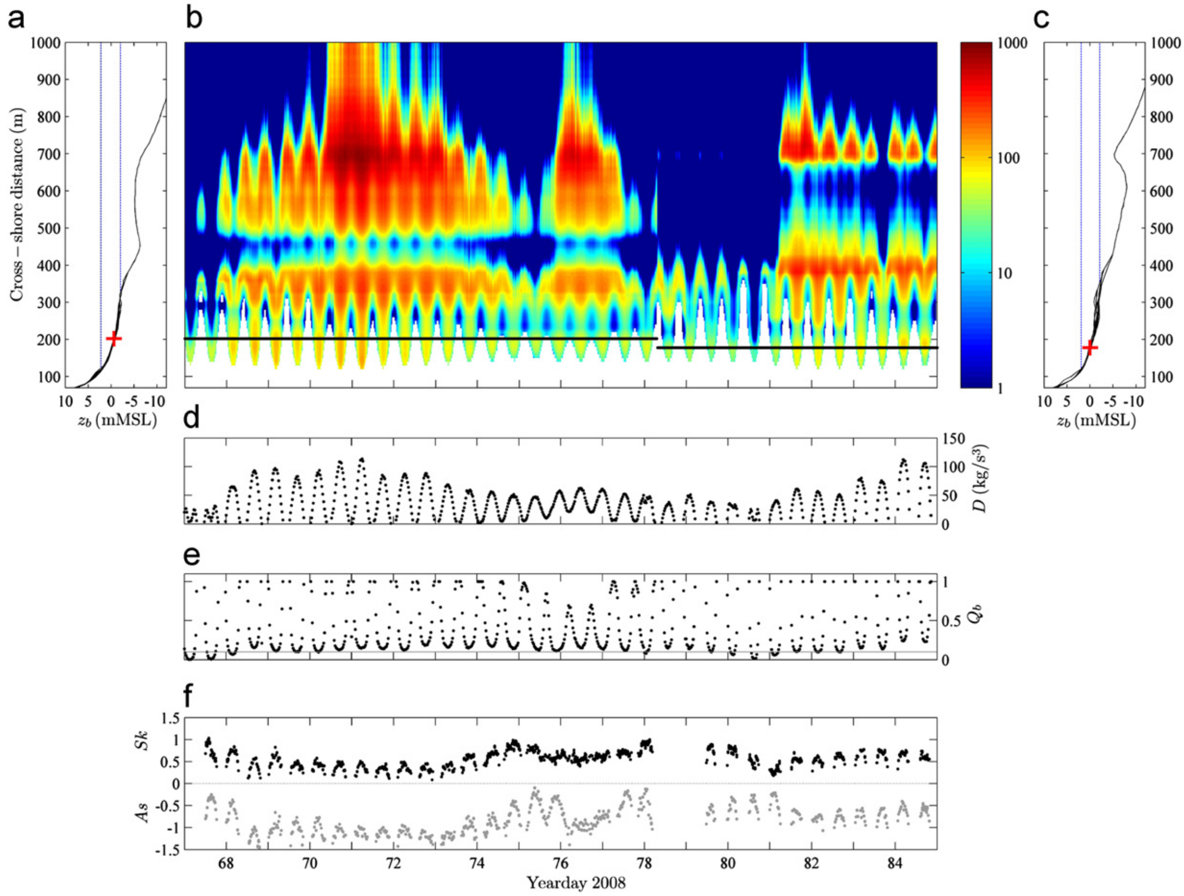

Fig. 5. Time evolution of (b) the cross-shore profiles of the simulated wave energy flux decay D, (d) local (at the rig) simulated wave energy flux decay D, (e) simulated percentage of breaking waves Q_b, and (f) measured wave skewness Sk and asymmetry As. In (b), the black line represents the cross-shore rig position. Panels (a) and (c) represent daily cross-shore beach profiles z_b with respect to chart datum during yeardays 67–78.3 and yeardays 78.3–85, respectively. Blue-dotted lines represent low and high tide levels; red crosses are rig positions. In (e), the horizontal gray line corresponds to $Q_b = 10\%$. (For interpretation of the references to color in this figure caption, the reader is referred to the web version of this article.)

depth modulated ($D < 150\ \mathrm{kg/s^3}$, Fig. 5d); waves reformed after the inner bar and most of them were breaking or broken at the rig. This is confirmed by the predicted percentage of breaking waves Q_b (Fig. 5e), ranging from 10% in the outer part to 100% in the inner part of the intertidal dissipation zone.

2.2.3. Wave skewness and asymmetry

Grasso and Ruessink (2011) suggested that temporal variability in the vertical ε structure was related to whether waves were breaking or propagated as bores. To distinguish between breaking-waves and bores, they used the ratio H_s/h. A more appropriate way to distinguish both wave types may be to use the wave shape, where bores are more pitched forward than breaking waves (e.g., Ogston and Sternberg, 2002). The wave shape can be evaluated by means of higher order moments of the sea surface elevation, such as wave skewness, Sk, and wave asymmetry, As. The skewness and asymmetry are statistical measures of the horizontal (peaked) and vertical (pitched forward) asymmetry of the wave form, respectively. They read

$$Sk = \frac{\langle (\eta - \langle \eta \rangle)^3 \rangle}{\langle (\eta - \langle \eta \rangle)^2 \rangle^{3/2}} \tag{2}$$

$$As = \frac{\langle \mathcal{H}^3 (\eta - \langle \eta \rangle) \rangle}{\langle (\eta - \langle \eta \rangle)^2 \rangle^{3/2}} \tag{3}$$

where $\langle \cdot \rangle$ represents a burst average operator and $\mathcal{H}$ is the Hilbert transform. These parameters evolve with h and hence location within the surf zone (e.g., Elgar and Guza, 1985; Doering and Bowen, 1995; Elgar et al., 2001; Grasso et al., 2011; Michallet et al., 2011). Very recently, Ruessink et al. (in press) proposed a wave shape parametrization for natural irregular waves and showed that a Sk–As couple can be related uniquely to a cross-shore location in the nearshore (depending on local H_s, h and period T). Breaking waves are mainly skewed and slightly asymmetric while Sk decreases and $|As|$ increases (where $|\cdot|$ is the absolute operator) under bores. Estimates at the rig ($Sk = 0.15 - 1$ and $|As| = 0.1 - 1.3$, Fig. 5f) are consistent with waves at being breaking or bores. Combining the Sk–As observations with SWAN's Q_b predictions, we observe that waves are mainly breaking for $Sk > |As|$ ($Q_b \approx 10 - 20\%$) in the outer part of the intertidal dissipation zone and are bores for $Sk < |As|$ ($Q_b \approx 50 - 100\%$) in the inner part. These latter conditions were observed for several consecutive days within cross-shore extensive surf zones during high-energy wave conditions (e.g., yeardays 70–73) and for a few hours during low tides otherwise.

3. Results and discussion

To identify the dominant vertical ε structure, the 167ε profiles were decomposed into three Empirical Orthogonal Functions

(EOFs) (e.g., Von Storch and Zwiers, 1999)

$$\varepsilon(i,t) = \sum_{j=1}^{3} a_j(t)E_j(i) \qquad (4)$$

here i refers to the ADVO instrument ($i=1$, 2, 3), $E_j(i)$ are the (nondimensional) EOFs representing fixed vertical patterns ($\mathbf{E}^{\mathbf{T}}\mathbf{E}=\mathbf{I}$, where $\mathbf{E}^{\mathbf{T}}$ is the transpose of $\mathbf{E}$ and $\mathbf{I}$ is the identity matrix), and $a_j(t)$ are the (dimensional) temporal EOF coefficients. The first EOF contained 97% of the ε variance, indicating that the temporal variations in ε were highly coherent in the water column, and decreased toward the bed (Fig. 6a). The EOF coefficients depended positively on H_{tot}/h (Fig. 6b), with a log correlation of $r^2=0.64$, whereas they were correlated poorly to H_s/h ($r^2=0.3$). Thus H_{tot}/h, which includes infragravity waves, may be a better proxy for the shallow-water turbulence intensity than H_s/h. Interestingly, the EOF coefficients were not significantly related to the water depth (Fig. 6c), implying that the positive dependence on H_{tot}/h is not simply due to a reduction in h. The positive ε sign and its vertical structure indicate that wave breaking is the dominant source of turbulence in the water column. The vertical ε structure observed here differs from that observed by Feddersen et al. (2007) under whitecapping wave breaking. In their case, ε peaked near the surface and at the bed, revealing distinctly both surface- and bed-generated turbulence. Finally, we note that the EOF coefficients were also well related to the wave shape, as they increased positively with $|As|$ and negatively with Sk (Fig. 6d). Thus, the magnitude of ε increased under asymmetric waves (bores).

To analyze further the vertical ε structure, we decomposed ε in three domains corresponding to different wave breaking conditions, based on the wave shape analysis (Fig. 5b, e and f). As presented in Fig. 7, H_{tot}/h was well related to the wave shape and can thus be used in our study for defining different breaking conditions (see Section 2.2.3). (i) For $H_{tot}/h=0.4-0.675$, Sk exceeds $|As|$, representative of breaking waves; (ii) for $H_{tot}/h=0.675-0.825$, Sk and $|As|$ are about the same, representative of a transition zone between breaking waves and bores; and (iii) for $H_{tot}/h=0.825-1.3$, $|As|$ is larger than Sk, representative of bores. Fig. 8a shows the first EOF time-averaged, $E_1(i)\times\overline{a_1(t)}$, which explain 94%, 96%, and 93% of the variance of ε under breaking waves, in the transition zone, and under bores, respectively. Here, $\overline{(\cdot)}$ represents averaging over all observations. The turbulent dissipation rate was almost depth-uniform under breaking waves, whereas it decreased profoundly toward the bed under bores, implying that most of the wave-breaking turbulence is dissipated near the surface under bores. This validates the hypothesis of Grasso and Ruessink (2011) that the change from breaking waves to bores alters the structure of ε in the water column. The vertical ε

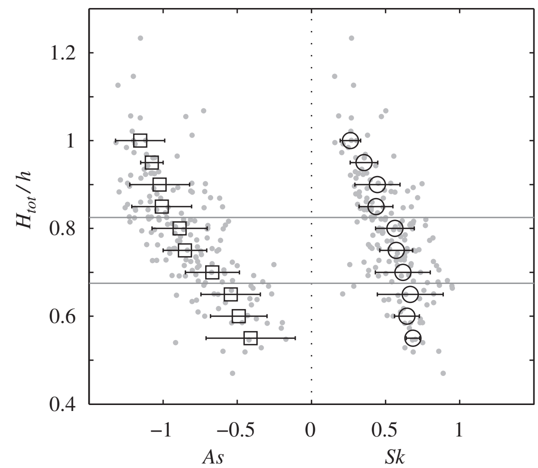

Fig. 7. The total relative wave height H_{tot}/h versus wave skewness Sk and asymmetry As. Circles and squares represent class-mean values $\overline{Sk}$ and $\overline{As}$, respectively, according to $H_{tot}/h\pm0.05$; the horizontal brackets are ±1 standard deviation. Symbols and bars are shown only when the number of observations in a H_{tot}/h bin exceeded 5. The two horizontal gray lines delimit the three domains: $H_{tot}/h=0.4-0.675$ for $\overline{Sk}>|\overline{As}|$ (breaking waves); $H_{tot}/h=0.675-0.825$ for $0.5<\overline{Sk}$, $|\overline{As}|<1$ (transition zone); and $H_{tot}/h=0.825-1.3$ for $\overline{Sk}<0.5$ and $|\overline{As}|>1$ (bores).

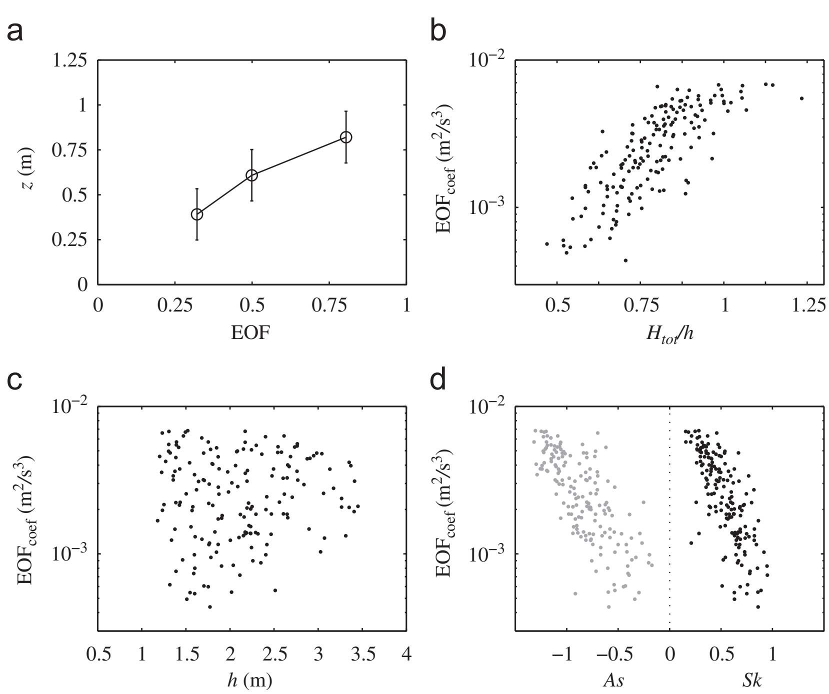

Fig. 6. EOF decomposition of ε. (a) The vertical structure of the first EOF $E_1(i)$. The temporal coefficients of the first EOF, $a_1(t)$, versus (b) the total relative wave height H_{tot}/h, (c) water depth h, and (d) wave skewness Sk and asymmetry As. In (a), the vertical brackets are ±1 standard deviation.

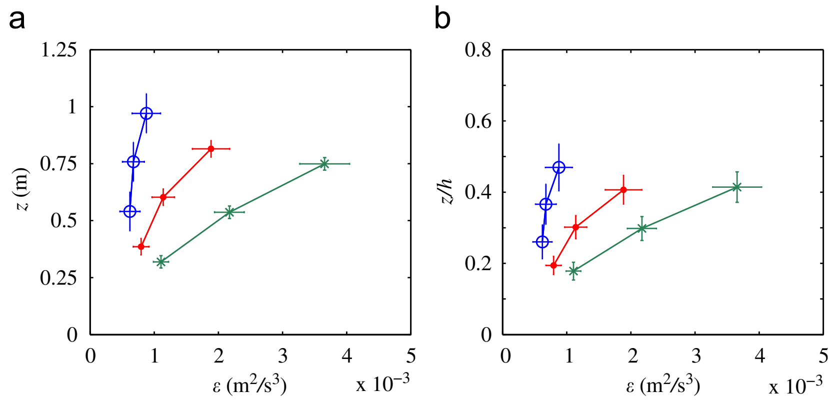

Fig. 8. First EOF derived structure of ε, $E_1(i)\times\overline{a_1(t)}$, versus (a) the elevation above the bed z and (b) the relative vertical position z/h, for different wave breaking conditions: breaking waves ($H_{tot}/h=0.4-0.675$, circles), transition zone ($H_{tot}/h=0.675-0.825$, dots), and bores ($H_{tot}/h=0.825-1.3$, crosses). Horizontal and vertical brackets represent the 99% confidence intervals.

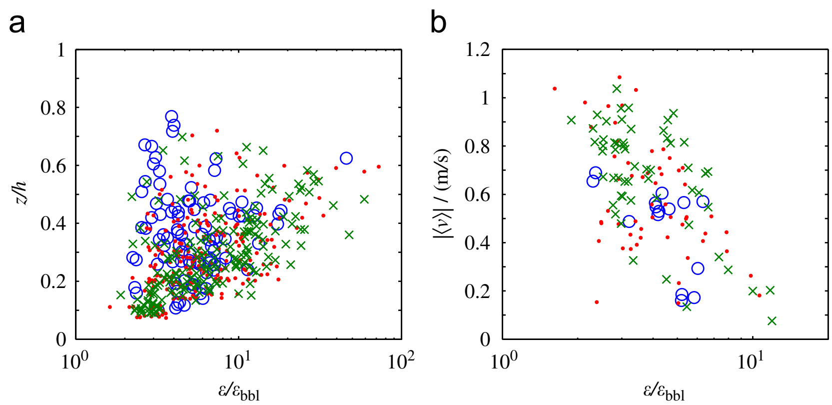

Fig. 9. Non-dimensional dissipation rates $\varepsilon/\varepsilon_{\rm bbl}$ versus (a) the relative vertical position z/h and (b) the mean alongshore velocities $|\langle v\rangle|$ for different wave breaking conditions: breaking waves ($H_{tot}/h=0.4-0.675$, circles), transition zone ($H_{tot}/h=0.675-0.825$, dots), and bores ($H_{tot}/h=0.825-1.3$, crosses). In (b), only near-bed measurements ($z/h<0.2$) are shown.

structures we observed here are very similar to the vertical variations from the outer to the inner surf zone observed across a barred beach in the laboratory (Yoon and Cox, 2010). The vertical ε structures with regard to the relative position in the water column z/h ($z/h=0$ at the sea bed, $z/h=1$ at the sea surface, and the wave-trough level is at z/h=0.7–0.8, depending on wave conditions) are similar to those as a function of z only (compare Fig. 8b with Fig. 8a). Hence in the intertidal dissipation zone, neither the ε magnitude (Fig. 6c) nor its vertical structure are determined by h only.

To analyze the importance of the bed-generated turbulence in the intertidal dissipation zone, we compare ε with the turbulent dissipation rate induced by current friction at the bed, $\varepsilon_{\rm bbl}$. Following Feddersen et al. (2007), we estimated $\varepsilon_{\rm bbl}$ from the data using

$$\varepsilon_{\rm bbl}=u_*^3/\kappa z \tag{5}$$

where $u_*=[C_d\langle|U|v\rangle]^{1/2}$ is the bed friction velocity. $|U|=(u^2+v^2)^{1/2}$, where u and v are the instantaneous horizontal velocities, $\kappa=0.4$ is the empirical Von Kármán's constant, and $C_d=1.6\times10^{-3}$ is a constant inferred by Ruessink (2010) for the same dataset. As detailed in Ruessink (2010), $C_d=1.6\times10^{-3}$ was estimated at z/h=0.08–0.12 and decreased toward the surface. Fig. 9a illustrates the ratio $\varepsilon/\varepsilon_{\rm bbl}$ as a function of z/h for the three wave-breaking conditions. Close to the bed ($z/h\approx0.1$), ε was at least 2–3 times larger than $\varepsilon_{\rm bbl}$ and could be up to 70 times larger closer to the surface ($z/h\approx0.6$). In contrast to flume experiments, our results were obtained during strong alongshore currents (up to $|\langle v\rangle|=1.13$ m/s) because of quasi-persistent high-energy offshore oblique waves (Almar et al., 2010). Within the lower 20% of the water column ($z/h<0.2$), $\varepsilon/\varepsilon_{\rm bbl}$ decreased significantly with $|\langle v\rangle|$ (Fig. 9b). Hence, the relative importance of $\varepsilon_{\rm bbl}$ increased from $\approx$10% for $|\langle v\rangle|\approx0.1$ m/s to $\approx$50% for $|\langle v\rangle|\approx1$ m/s.

Because bed-generated turbulence appears to be subordinate to breaking-induced turbulence, we continue with quantifying the fraction of wave energy flux decay dissipated in the water column. Following Svendsen (1987), we take

$$\varepsilon_{\rm D}=D/\rho h \tag{6}$$

as the depth-averaged breaking-induced dissipation rate (ρ is the water density). The fraction of $\varepsilon_{\rm D}$ dissipated below wave-trough level is $\varepsilon/\varepsilon_{\rm D}$. Fig. 10 illustrates the ratio $\varepsilon/\varepsilon_{\rm D}$ as a function of z/h for the three wave breaking conditions. Just below wave-trough level ($z/h\approx0.6$), $\varepsilon/\varepsilon_{\rm D}$ ranged from $\approx$1%, mainly under breaking waves, to $\approx$20%, mainly under bores. Close to the bed ($z/h\approx0.1$), $\varepsilon/\varepsilon_{\rm D}$ varied only between $\approx$2 and 8% and remained somewhat larger under bores. By depth-integration, we found that approximately 1–10% of the breaking-induced dissipation (D/ρ) was dissipated in the water column. This agrees well with estimates of 2–6% in the laboratory experiments compiled by Svendsen (1987), and with estimates of 1% in the outer surf zone, increasing to about 10–12% under bores in the laboratory experiments of Huang et al. (2009). Interestingly, ε within the water column increases from breaking waves to bores (Fig. 8), while the wave energy decay at the surface, D, decreases (Fig. 5d). This leads to

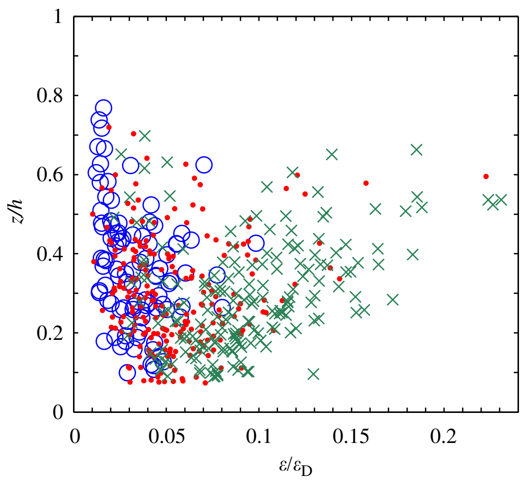

Fig. 10. Non-dimensional dissipation rates $\varepsilon/\varepsilon_D$ versus the relative vertical position z/h for different wave breaking conditions: breaking waves ($H_{tot}/h = 0.4-0.675$, circles), transition zone ($H_{tot}/h = 0.675-0.825$, dots), and bores ($H_{tot}/h = 0.825-1.3$, crosses).

the larger relative turbulence dissipation rate, $\varepsilon/\varepsilon_D$, below wave-trough level under bores, as observed in Fig. 10, compare circles and crosses.

4. Conclusions and implications

We analyzed the turbulence dissipation rate, ε, in a natural surf zone below the wave-trough level. We used wave shape and wave energy decay estimates to distinguish breaking waves and bores in the outer and inner part of the intertidal dissipation zone, respectively. The total relative wave height (H_{tot}/h), which includes infragravity waves, is well related to wave breaking conditions and represents a pertinent proxy for ε estimates. The vertical ε structure indicates that wave breaking is the dominant source of turbulence and that the ε magnitude increases with H_{tot}/h, i.e. from breaking waves to bores. Under breaking waves, ε is almost depth-uniform, whereas it decreases profoundly toward the bed under bores, implying that most of the breaking-induced turbulence is dissipated near the surface under bores. We found that ε estimates were at least 2 times larger than current-induced turbulent dissipation rates, even when alongshore currents were ≈ 1 m/s. The data further illustrate that the fraction of wave energy flux decay dissipated below wave-trough level ranged from $\approx 1\%$ under breaking waves to $\approx 10\%$ under bores, confirming previous laboratory results.

The results of this study imply that coastal-evolution models considering only the sea-bed turbulence source severely underestimate the turbulence dissipation rate in the surf zone and hence are likely to underestimate sand stirring and the magnitude of sand concentration in the water column (cf. Deigaard et al., 1986; Roelvink and Stive, 1989). This will assuredly cause the sand transport by mean currents to be underestimated during severe storms. We anticipate that our results will help to extend and validate turbulence models and will eventually result in more accurate beach-erosion predictions. Further work is necessary to establish the link between sand suspension events and individual turbulence bursts (cf. Scott et al., 2009) under natural conditions.

Acknowledgments

The field data were collected as part of the multi-institutional ECORS (SHOM-DGA) project. We are greatly indebted to Marcel van Maarseveen, Henk Markies, and Bas van Dam for the electronic and mechanic design of the rig and their excellent field support. We thank M. Tissier from the EPOC laboratory (France), and J. Brown and J. MacMahan from the Naval Postgraduate School (CA, USA), supported by the National Science Foundation OCE 0728324, for providing us with the wave height measurements used to validate SWAN predictions. In addition, we acknowledge J.-R. Grasso, T. Price, R. T. Guza, F. Feddersen and the two anonymous reviewers for providing useful feedback on this work. Funded by the French Ministry of Defence (DGA/DS) under project 2009.60.077 and by the Netherlands Organisation for Scientific Research NWO (Rubicon/Marie Curie Cofund Action) under project 825.10.034. BC was additionally funded by BARBEC (ANR 2010 JCJC 602 01).

References

Aagaard, T., Hughes, M.G., 2010. Breaker turbulence and sediment suspension in the surf zone. Marine Geology 271, 250–259.
Almar, R., Castelle, B., Ruessink, B.G., Sénéchal, N., Bonneton, P., Marieu, V., 2010. Two- and three-dimensional double-sandbar system behaviour under intense wave forcing and meso-macro tidal range. Continental Shelf Research 30, 781–792.
Booij, N., Ris, R.C., Holthuijsen, L.H., 1999. A third-generation wave model for coastal regions. 1. Model description and validation. Journal of Geophysical Research 104 (C4), 7649–7666.
Bryan, K.R., Black, K.P., Gorman, R.M., 2003. Spectral estimates of dissipation rate within and near the surf zone. Journal of Physical Oceanography 33, 979–993.
Deigaard, R., Fredsøe, J., Hedegaard, I.B., 1986. Suspended sediment in the surf zone. Journal of Waterway, Port, Coastal, and Ocean Engineering, ASCE 112, 115–128.
Doering, J.C., Bowen, A.J., 1995. Parametrization of orbital velocity asymmetries of shoaling and breaking waves using bispectral analysis. Coastal Engineering 26, 15–33.
Elgar, S., Gallagher, E.L., Guza, R.T., 2001. Nearshore sandbar migration. Journal of Geophysical Research 106, 11623–11628.
Elgar, S., Guza, R.T., 1985. Observations of bispectra of shoaling surface gravity-waves. Journal of Fluid Mechanics 161, 425–448.
Elgar, S., Raubenheimer, B., Guza, R.T., 2005. Quality control of acoustic doppler velocimeter data in the surf zone. Measurement Science and Technology 16, 1889–1893.
Feddersen, F., 2010. Quality controlling surf zone acoustic doppler velocimeter, observations to estimate the turbulent dissipation rate. Journal of Atmospheric and Oceanic Technology 27, 2039–2055.
Feddersen, F., Trowbridge, J.H., 2005. The effect of wave breaking on surf-zone turbulence and alongshore currents: a modeling study. Journal of Physical Oceanography 35 (11), 2187–2203.
Feddersen, F., Trowbridge, J.H., Williams III, A.J., 2007. Vertical structure of dissipation in the nearshore. Journal of Physical Oceanography 37, 1764–1777.
George, R., Flick, R.E., Guza, R.T., 1994. Observations of turbulence in the surf zone. Journal of Geophysical Research 99 (C1), 801–810.
Gerbi, G.P., Trowbridge, J.H., Terray, E.A., Plueddemann, A.J., Kukulka, T., 2009. Observations of turbulence in the ocean surface boundary layer: energetics and transport. Journal of Physical Oceanography 39, 1077–1096.
Govender, K., Mocke, G.P., Alport, M.J., 2002. Video-imaged surf zone wave and roller structures and flow field. Journal of Geophysical Research 107 (C73072)http://dx.doi.org/10.1029/2000JC000755.
Govender, K., Mocke, G.P., Alport, M.J., 2004. Dissipation of isotropic turbulence and length-scale measurements through the wave roller in laboratory spilling waves. Journal of Geophysical Research 109 (C08018)http://dx.doi.org/10.1029/2003JC002233.
Grasso, F., Michallet, H., Barthélemy, E., 2011. Sediment transport associated with morphological beach changes forced by irregular asymmetric, skewed waves. Journal of Geophysical Research 116 (C03020)http://dx.doi.org/10.1029/2010JC006550.
Grasso, F., Ruessink, B.G., 2011. Vertical structure of turbulence dissipation in the shallow-water surf zone. Journal of Coastal Research SI64, 90–94.
Hsu, T.J., Elgar, S., Guza, R.T., 2006. Wave-induced sediment transport and onshore sandbar migration. Coastal Engineering 53, 817–824.
Huang, Z.C., Hsiao, S.C., Hwung, H.H., Chang, K.A., 2009. Turbulence and energy dissipations of surf-zone spilling breakers. Coastal Engineering 56, 733–746.
Kimmoun, O., Branger, H., 2007. A particle image velocimetry investigation on laboratory surf-zone breaking waves over a sloping beach. Journal of Fluid Mechanics 588, 353–397.
Kobayashi, N., Payo, A., Schmied, L., 2008. Cross-shore suspended sand and bed load transport on beaches. Journal of Geophysical Research 113 (C07001)http://dx.doi.org/10.1029/2007JC004203.
Michallet, H., Cienfuegos, R., Barthélemy, E., Grasso, F., 2011. Wave kinematics in propagation and breaking on a barred beach. European Journal of Mechanics—B/Fluids 30 (6), 624–634.

Mocke, G.P., 2001. Structure and modeling of surf zone turbulence due to wave breaking. Journal of Geophysical Research 106 (C8), 17039–17057.
Mori, N., Suzuki, T., Kakuno, S., 2007. Noise of acoustic doppler velocimeter data in bubbly flows. Journal of Engineering Mechanics 133, 122–125.
Nadaoka, K., Hino, M., Koyano, Y., 1989. Structure of the turbulent flow field under breaking waves in the surf zone. Journal of Fluid Mechanics 204, 359–387.
Nadaoka, K., Ueno, S., Igarashi, T., 1988. Sediment suspension due to large scale eddies in the surf zone. In: Proceedings of the 21st International Conference on Coastal Engineering. American Society of Civil Engineering, New York, NY, pp. 1646–1660.
Ogston, A.S., Sternberg, R.W., 2002. Effect of wave breaking on sediment eddy diffusivity, suspended-sediment and longshore sediment flux profiles in the surf zone. Continental Shelf Research 22, 633–655.
Ribberink, J.S., 1998. Bed-load transport for steady flows and unsteady oscillatory flows. Coastal Engineering 34, 59–82.
Ribberink, J.S., van der Werf, J.J., O'Donoghue, T., Hassan, W.N.M., 2008. Sand motion induced by oscillatory flows: sheet flow and vortex ripples. Journal of Turbulence 9 (20), 1–32.
Roelvink, J.A., Stive, M.J.F., 1989. Bar-generating cross-shore flow mechanisms on a beach. Journal of Geophysical Research 94 (C4), 4785–4800.
Ruessink, B.G., 2005. Predictive uncertainty of a nearshore bed evolution model. Continental Shelf Research 25, 1053–1069.
Ruessink, B.G., 2010. Observations of turbulence within a natural surf zone. Journal of Physical Oceanography 40, 2696–2712.
Ruessink, B.G., Kuriyama, Y., 2008. Numerical predictability experiments of cross-shore sandbar migration. Geophysical Research Letters 35 (L01603).
Ruessink, B.G., Kuriyama, Y., Reniers, A.J.H.M., Roelvink, J.A., Walstra, D.J.R., 2007. Modeling cross-shore sandbar behavior on the timescale of weeks. Journal of Geophysical Research 112 (F03010)http://dx.doi.org/10.1029/2006JF000730.
Ruessink, B.G., Michallet, H., Abreu, T., Sancho, F., van der A, D.A., van der Werf, J., Silva, P.A., 2011. Observations of velocities, sand concentrations, and fluxes under velocity-asymmetric oscillatory flows. Journal of Geophysical Research 116 (C03004)http://dx.doi.org/10.1029/2010JC006443.
Ruessink, B.G., Ramaekers, G., van Rijn, L.C., 2012. On the parameterization of the free-stream non-linear wave orbital motion in nearshore morphodynamic models. Coastal Engineering 65, 56–63.
Ruggiero, P., Walstra, D.J.R., Gelfenbaum, G., van Ormondt, M., 2009. Seasonal-scale nearshore morphological evolution: field observations and numerical modeling. Coastal Engineering 56, 1153–1172.
Scott, C.P., Cox, D.T., Maddox, T.B., Long, J.W., 2005. Large-scale laboratory observations of turbulence on a fixed barred beach. Measurement Science and Technology 16, 1903–1912.
Scott, N.V., Hsu, T.J., Cox, D., 2009. Steep wave, turbulence, and sediment concentration statistics beneath a breaking wave field and their implications for sediment transport. Continental Shelf Research 29, 2303–2317.
Sénéchal, N., Abadie, S., Gallagher, E., MacMahan, J., Masselink, G., Michallet, H., Reniers, A., Ruessink, B.G., Russell, P., Sous, D., Turner, I., Ardhuin, F., Bonneton, P., Bujan, S., Capo, S., Certain, R., Pedreros, R., Garlan, T., 2011. The ECORS-Truc Vert'08 nearshore field experiment: presentation of a three-dimensional morphologic system in a macro-tidal environment during consecutive extreme storm conditions. Ocean Dynamics 61, 2073–2098.
Silva, P.A., Temperville, A., Santos, F.S., 2006. Sand transport under combined current and wave conditions: a semi-unsteady practical model. Coastal Engineering 53, 897–913.
Svendsen, I.A., 1987. Analysis of surf zone turbulence. Journal of Geophysical Research 92 (C5), 5115–5124.
Thornton, E.B., 1979. Energetics of breaking waves within the surf zone. Journal of Geophysical Research 84 (C8), 4931–4938.
Ting, F.C.K., Kirby, J.T., 1995. Dynamics of surf-zone turbulence in a strong plunging breaker. Coastal Engineering 24 (3–4), 177–204.
Ting, F.C.K., Kirby, J.T., 1996. Dynamics of surf-zone turbulence in a spilling breaker. Coastal Engineering 27, 131–160.
Tissier, M., Bonneton, P., Almar, R., Castelle, B., Bonneton, N., Nahon, A., 2011. Field measurements and non-linear prediction of wave celerity in the surf zone. European Journal of Mechanics—B/Fluids 30, 635–641.
Trowbridge, J., Elgar, S., 2001. Turbulence measurements in the surf zone. Journal of Physical Oceanography 31, 2403–2417.
Van Rijn, L.C., Walstra, D.J.R., Grasmeijer, B., Sutherland, J., Pan, S., Sierra, J.P., 2003. The predictability of cross-shore bed evolution of sandy beaches at the time scale of storms and seasons using process-based profile models. Coastal Engineering 47, 295–327.
Von Storch, H., Zwiers, F.W., 1999. Statistical Analysis in Climate Research. Cambridge University Press.
Yoon, H.D., Cox, D.T., 2010. Large-scale laboratory observations of wave breaking turbulence over an evolving beach. Journal of Geophysical Research 115 (C10007)http://dx.doi.org/10.1029/2009JC005748.